New High-quality Strong Lens Candidates with Deep Learning in the Kilo-Degree Survey

R. Li[1], N. R. Napolitano[1] , C. Tortora[2] , C. Spiniello[3] , L. V. E. Koopmans[4] , Z. Huang[1] , N. Roy[1], G. Vernardos[4,5],
S. Chatterjee[4] , B. Giblin[6], F. Getman[3], M. Radovich[7] , G. Covone[3,8,9] , and K. Kuijken[10]

[1] School of Physics and Astronomy, Sun Yat-sen University, Zhuhai Campus, 2 Daxue Road, Xiangzhou District, Zhuhai, People's Republic of China
lirui228@mail.sysu.edu.cn, napolitano@mail.sysu.edu.cn
[2] Osservatorio Astrofisico di Arcetri, L.go E. Fermi 5, I-50125 Firenze, Italy
[3] INAF–Osservatorio Astronomico di Capodimonte, Salita Moiariello,16, I-80131 Napoli, Italy
[4] Kapteyn Astronomical Institute, University of Groningen, P.O. Box 800, 9700AV Groningen, The Netherlands
[5] Institute of Astrophysics, Foundation for Research and Technology–Hellas (FORTH), GR-70013, Heraklion, Greece
[6] Institute for Astronomy, University of Edinburgh, Blackford Hill, Edinburgh, EH9 3HJ, UK
[7] INAF–Osservatorio Astronomico di Padova, Vicolo Osservatorio 5, I-35122 Padova, Italy
[8] Dipartimento di Fisca "E. Pancini," University of Naples "Federico II," Naples, Italy
[9] INFN, Sezione di Napoli, Naples, Italy
[10] Leiden Observatory, Leiden University, P.O. Box 9513, 2300 RA Leiden, The Netherlands

Abstract

We report new high-quality galaxy-scale strong lens candidates found in the Kilo-Degree Survey data release 4 using machine learning. We have developed a new convolutional neural network (CNN) classifier to search for gravitational arcs, following the prescription by Petrillo et al. and using only *r*-band images. We have applied the CNN to two "predictive samples": a luminous red galaxy (LRG) and a "bright galaxy" (BG) sample ($r < 21$). We have found 286 new high-probability candidates, 133 from the LRG sample and 153 from the BG sample. We have ranked these candidates based on a value that combines the CNN likelihood of being a lens and the human score resulting from visual inspection (*P*-value), and here we present the highest 82 ranked candidates with *P*-values $\geqslant 0.5$. All of these high-quality candidates have obvious arc or pointlike features around the central red defector. Moreover, we define the best 26 objects, all with *P*-values $\geqslant 0.7$, as a "golden sample" of candidates. This sample is expected to contain very few false positives; thus, it is suitable for follow-up observations. The new lens candidates come partially from the more extended footprint adopted here with respect to the previous analyses and partially from a larger predictive sample (also including the BG sample). These results show that machine-learning tools are very promising for finding strong lenses in large surveys and more candidates can be found by enlarging the predictive samples beyond the standard assumption of LRGs. In the future, we plan to apply our CNN to the data from next-generation surveys such as the Large Synoptic Survey Telescope, Euclid, and the Chinese Space Station Optical Survey.

Unified Astronomy Thesaurus concepts: Gravitational lensing (670); Strong gravitational lensing (1643); Dark matter (353); Elliptical galaxies (456)

1. Introduction

Strong lensing (SL) is the effect of the deformation of images of background galaxies due to the bending of their light rays from the gravitational potential of foreground systems acting as lenses or "deflectors" (usually massive luminous galaxies or galaxy groups/clusters). This effect, predicted by general relativity, manifests itself as spectacular arcs or rings (the so-called Einstein rings) around massive galaxies when the source is extended. In case of pointlike objects, such as high-redshift quasars, multiple images of the sources are created (mupols) instead.

To gain insight into the dark matter distribution in galaxies, SL is a powerful tool (Refsdal 1964; Blandford & Narayan 1992; Schneider et al. 1992; Keeton 1998; Congdon & Keeton 2018). For instance, it can be used in combination with dynamical analysis to determine the total mass density profiles of the lens systems (e.g., Koopmans et al. 2006, 2009; Auger et al. 2010; Bolton et al. 2012; Li et al. 2018). In case an independent inference on the stellar mass of the deflectors is available, e.g., via stellar population analysis, SL also allows one to directly measure the amount and properties of the internal dark matter of the deflectors (e.g., Koopmans et al. 2006; Auger et al. 2009; Tortora et al. 2010; Spiniello et al. 2011; Barnabè et al. 2012;

Shu et al. 2015; Gilman et al. 2018; Nightingale et al. 2019; Schuldt et al. 2019).

In addition, SL can be used to measure the Hubble constant, H_0, as well as other cosmological parameters (e.g., Refsdal 1964; Suyu et al. 2013; Sluse et al. 2019). In particular, this is possible by measuring the luminosity variation of lensed quasars and using the time delay of the occurrence of their peak luminosity, which is highly sensitive to H_0 and a little sensitive to other parameters (see, e.g., the H0LiCOW project; Bonvin et al. 2017; Suyu et al. 2017). Combining the inference obtained by more than one lens system, it has been possible to decrease the error on the measurement of H_0 to 2.4% (Wong et al. 2020). This number is likely to decrease by further increasing the number of systems used to infer it.

Additionally, SL can be used to check the gravity theory by measuring the difference between gravitational lensing mass and dynamical mass (e.g., Schwab et al. 2010; Cao et al. 2017; Collett et al. 2018), and it can help to search for lower-mass dark substructures around larger galaxies and then constrain the dark matter model (e.g., Vegetti et al. 2012; Li et al. 2017; Hsueh et al. 2020). Finally, SL can be treated as a "natural" telescope to study very faint high-redshift galaxies that are otherwise impossible to directly detect with an artificial

telescope (e.g., ALMA Partnership et al. 2015; Cornachione et al. 2018; Chen et al. 2019; Claeyssens et al. 2019; Rydberg et al. 2020).

The probability that a distant source is lensed to produce multiple images or arcs is very small (Turner et al. 1984; Fukugita et al. 1992). For instance, Dobler et al. (2008) estimated that the galaxy–galaxy lens candidate rate in the Sloan Digital Sky Survey spectroscopic data is ∼0.5%–1.3%. Updated predictions based on ΛCDM cosmology suggest that, in ground-based high-resolution large sky surveys, between 0.5 and 10 lenses deg^2 can be found, depending on the source nature (e.g., distant pointlike quasars or extended galaxies), depth, and survey strategy (Oguri & Marshall 2010; Collett 2015).

Thus, to collect statistical samples of lensing systems, one needs to start from a very large number of galaxies and thus use wide-sky large surveys. As a matter of fact, more than 1000 new lens candidates have been found in the last 3 yr in recent ground-based surveys (e.g., Jacobs et al. 2017, 2019; Petrillo et al. 2017, 2019b; Pourrahmani et al. 2018; Khramtsov et al. 2019), such as the Kilo-Degree Survey (KiDS; de Jong et al. 2013), Hyper Suprime-Cam Subaru Strategic Program (HSC; Miyazaki et al. 2012), and Dark Energy Survey (DES; The Dark Energy Survey Collaboration 2005). So far, a few hundred systems have been confirmed (e.g., Bolton et al. 2008; Brownstein et al. 2012; Treu & SWELLS Team 2012; Sonnenfeld et al. 2013; Shu et al. 2016, 2017; Agnello et al. 2018; Spiniello et al. 2018, 2019; Agnello & Spiniello 2019; Lemon et al. 2020).

However, despite these large numbers, the known lenses are still far from enough, especially for studies that need large statistical samples. This is particularly important in the case of distant quasars producing four multiple images (quadruplets), which are the ideal systems for cosmography. These are, unfortunately, also the rarest cases, representing only 10%–20% of the full population of mupols. The error of H_0 measured from a single lensed quasar is extremely sensitive to the mass distribution of its defector. Since this error is hard to reduce under 10% (see Kochanek 2020), the only way to further bring down the uncertainty is to combine the analysis on a large number of systems (see, e.g., H0LiCOW project; Suyu et al. 2013). The conditio sine qua non is therefore to find and confirm new lenses, and, in recent years, we have exploited the high-quality imaging offered by KiDS to find as many previously undiscovered gravitational lenses as possible, both arcs and mupols (e.g., Hartley et al. 2017; Petrillo et al. 2017, 2019a, 2019b; Spiniello et al. 2018, 2019; Khramtsov et al. 2019).

However, searching for strong lenses in a very large number of galaxies is a challenging task, and it will become even more challenging with the advent of next-generation sky surveys. In fact, thanks to their large survey areas and deeper limiting magnitudes, upcoming surveys will effectively increase the number of lens candidates up to ∼10^5 and even further (Collett 2015). For instance, the optical Large Synoptic Survey Telescope (LSST; Closson Ferguson et al. 2009), which will start in 2020 and cover 18,000 deg^2 in the Southern Hemisphere, is expected to find up to 120,000 lenses during its operations (Collett 2015). The space-based telescope Euclid (Amendola et al. 2018), with a point-spread function (PSF) of $0''2$ and sky areas of 15,000 deg^2, will find almost 170,000 arcs and mupols (Collett 2015). A comparable number of lenses will also be discovered by the Chinese Space Station Telescope (CSST; Zhan 2018), which will be launched in 2024 and is expected to cover 17,500 deg^2 with a PSF ∼$0''15$.

Traditionally, different methods, such as spectroscopic selections (e.g., Bolton et al. 2006, 2008), morphological recognition (e.g., Seidel & Bartelmann 2007; More et al. 2016) and crowd-sourcing methods (e.g., Marshall et al. 2016), have been used to optimize the detection efficiency. However, these methods will not be adequate for next-generation surveys, since the number of galaxies that will be observed will raise dramatically, making the manual identification and selection of lens candidates impossible.

Currently, machine learning (ML; Michalski 1986; Ivezić et al. 2014) appears to be the only viable alternative to human visual inspection to perform the lensing search task. This has already been shown in a number of pioneering works that have used ML techniques to search for strong lenses in some of the most successful ongoing sky surveys (e.g., Agnello et al. 2015; Hartley et al. 2017; Jacobs et al. 2017, 2019; Pourrahmani et al. 2018). In particular, our team has already actively participated in developing an ML-based routine to search for new SL in KiDS (e.g., Petrillo et al. 2017, 2019a, 2019b; Spiniello et al. 2018, 2019; Khramtsov et al. 2019). Furthermore, the Strong Gravitational Lens Finding Challenge (Metcalf et al. 2019), which has compared several lensing searching methods, also demonstrated that ML methods perform as well as human inspection or other traditional methods but with a much faster classification speed. The general result is that thousands of new lens candidates have been found with ML methods, quickly catching up with the total number of gravitational lenses collected from traditional methods over decades.

In this context, and preparing for the big lens-finding challenge with future all-sky surveys, we have started to investigate how to improve the completeness and purity of the candidates found by ML algorithms. In particular, in this paper, we present a new convolutional neural network (CNN) classifier to search for gravitational arcs and mupols and applied it to the r-band KiDS images. We have followed the prescription by Petrillo et al. (2019a, hereafter P19) and developed a CNN with the same architecture but using a different training set. Furthermore, we have applied it to a larger data set of preselected galaxies (for more detail about the differences, we refer the reader to Section 4), which allowed us to increase the number of high-quality lens candidates while recovering almost all of the lens candidates found from previous CNN of P19.

This is a preparatory work for the upcoming KiDS data release 5 (DR5; covering the full 1350 deg^2) and future programs with LSST, Euclid, and CSST. The paper is organized as follows. In Section 2, we describe the adopted CNN model and how we have selected the predictive data and training sample. In Section 3, we apply our CNN classifier to the predictive data and present the new findings. In Sections 4 and 5, we offer a discussion and summarize our main conclusions.

2. A New CNN Classifier for KiDS

The CNNs are one of the most popular ML models. Compared to traditional neural networks, the most important feature of CNNs is the use of convolution kernels as artificial neurons, which can effectively capture local features, making the CNNs particularly suitable for image recognition, speech

recognition, natural language processing, and some other tasks (Lecun et al. 1998). They are composed of a stack of distinct layers, such as the convolutional (used to extract different features of the inputs), pooling (used to compress the feature maps and simplify the calculations), and fully connected (used to turn all the local feature maps into a global feature map) layers. For more information about CNNs, we refer the reader to our previous paper (Li et al. 2019) or the recent review from Rawat & Wang (2017). In general, any good CNN model learns from the training data, provided that they are sufficient and suitable for the classification, and then makes predictions on the predictive data.

In this work, we used a CNN to search for gravitational lenses from a large sample of $\sim 10^6$ bright galaxies (BGs) and $\sim 10^5$ red luminous galaxies (see Section 2.1). This ML-based searching method is quite recent, and the best architecture to choose to optimize the SL finding is not yet understood. For this reason, we have compared the performances of different architectures, such as AlexNet (Krizhevsky & Sutskever 2012), ResNet (He et al. 2015), and a more recent one named DenseNet (Huang et al. 2016), to optimize the tool for the lensing search. As result, we decided to use a ResNet model with 18 convolutional layers, which best balanced performance and speed. For instance, AlexNet required less training time but returned a lower precision than ResNet, while DenseNet showed the opposite behavior. Also, deeper ResNets (e.g., 34 or 50 layers) are expected to have better performances but are more time-consuming.

The same choice was already made in P19, with which we share the core part of the classifier, coming from the same open-source code keras-resnet.[11] Therefore, there are no architectural differences between our classifier and that presented in P19. Furthermore, the classifiers are both built with Keras[12] and run on the back end of TensorFlow.[13] Despite the similarities between the two CNNs, the new classifier has been able to find more candidates. As we will explain in the following, this is mainly because of the different training sample used to train the CNN and the different predictive data on which we applied it.

2.1. The Predictive Data

Predictive data are systems over which the trained CNN can return a probability, $p_{\rm CNN}$ (i.e., make a prediction), of being a real lens (true positive). In principle, all targets detected in a survey can be part of the predictive sample. However, it makes no sense to feed the CNN with stars, quasars, low-redshift dwarf galaxies, or other very faint galaxies because they cannot act as gravitational lenses. Thus, a preselection can be done a priori to help reduce the computation time and potential contamination. Since the SL cross section is larger for massive galaxies (see, e.g., Oguri & Marshall 2010), a standard approach consists of using only the brighter and more massive systems as the predictive data.

To build our predictive data, we used the 1006 publicly available tiles from the latest KiDS data release, DR4. This contains a multiband optical catalog extracted from images in four optical bands (u, g, r, and i). Here we used only the r-band observations, since they have the best seeing with a median

FWHM of $\sim 0\rlap{.}{''}7$ (Kuijken et al. 2019). In an upcoming paper, we will further improve the results by exploiting g, r, and i color-composite images, hence using information on the colors for both the lens and the arcs/mupols, together with arc morphology and image positions. However, this has to be done in a careful way, and only if a proper training sample, well describing the population of real galaxies and their color distribution, is available. In fact, the lens colors can be contaminated by the presence of the source and, thus, not match a simple color cut designed to select LRGs.

The total number of detected sources in the publicly available KiDS DR4 catalog is ~ 120 million, of which more than 60 million are galaxies with high-quality photo-z obtained with the BPZ code[14] (see Kuijken et al. 2019). Among these, more than 5 million also have structural parameters from a seeing-convolved 2D single Sérsic model (see Roy et al. 2018 for the analysis of KiDS DR2).

In this work, we applied our CNN classifier to two predictive data sets. The first data set (referred to as the LRG sample) comprises only luminous red galaxies (LRGs), which are more likely to exhibit SL features, being generally more massive. Therefore, they are commonly used as a standard preselection sample in arc-finding searches (Wong et al. 2013; Petrillo et al. 2017, 2019b; P19). In addition, as a second predictive data set, we added a much larger sample of BGs (referred to as the BG sample) without any color cut. This is for two main reasons: (1) the color cuts to define LRGs are arbitrary and might not be optimal in the case of SL, where the lensed images can contaminate the colors of the lens (especially in cases where the Einstein radius is small); and (2) SL can be produced by distant massive galaxies, regardless their morphology/color.

Furthermore, the fastest GPUs today allow us to analyze a larger amount of data with almost no increase in the total computing time (see, e.g., Abadi et al. 2016). Of course, even if adding the BGs to the predictive sample increases the chance of finding new lenses, at the same, this also causes a larger contamination from false positives.

We give a description of the two predictive samples as follows.

1. BG sample. In the KiDS catalog, the BG sample has been chosen by (1) selecting galaxy-like objects using the flag `SG2DPHOT = 0` (this flag is derived with the software `2DPHOT` (La Barbera et al. 2008), which performs a star–galaxy separation in the KiDS catalog extraction process (see Kuijken et al. 2019, for KiDS DR4) and assigns a zero value to galaxies and values larger than zero to pointlike objects) and (2) requiring the r-band Kron-like magnitude `mag_auto` (also present in the KiDS catalogs and obtained by SExtractor; Bertin & Arnouts 1996) to be $r_{\rm auto} \leqslant 21$. The final BG sample selected with these two criteria consists of 3,808,963 galaxies.

2. LRG sample. The LRG predictive sample is a subsample of the BG sample, where we have followed the approach from P19, slightly adapted the low-redshift ($z < 0.4$) LRG color–magnitude selection in Eisenstein et al. (2001) to include fainter and bluer sources,

$$r_{\rm auto} < 14 + c_{\rm par}/0.3,$$
$$|c_{\rm perp}| < 0.2, \tag{1}$$

---

[11] https://github.com/raghakot/keras-resnet

[12] https://github.com/keras-team/keras

[13] https://github.com/tensorflow/tensorflow

[14] http://www.stsci.edu/~dcoe/BPZ/

where

$$c_{\mathrm{perp}} = (r - i) - (g - r)/4.0 - 0.18,$$
$$c_{\mathrm{par}} = 0.7(g - r) + 1.2[(r - i) - 0.18], \quad (2)$$

where r_{auto} is the r-band Kron-like magnitude as above. We restricted the selection to $r_{\mathrm{auto}} \leqslant 20$ for LRGs to match the P19 prescription. Galaxy colors have been directly retrieved by the KiDS DR4 catalogs from the flags COLOUR_GAAP_g_r ($=g - r$) and COLOUR_GAAP_r_i ($=r - i$). These colors are different from the ones used in Petrillo et al. (2017 2019a, 2019b), which were based on Kron-like magnitudes. In fact, Kron-like magnitudes in other bands are no longer listed in the KiDS catalog after KiDS DR3; thus, they are not publicly available for all sources in DR4. On the other hand, the COLOUR_GAAP was measured on Gaussian-weighted apertures, which are modified per-source and per-image, so they provide seeing-independent flux estimates across different observations/bands, hence providing more unbiased colors (Kuijken et al. 2019; P19). Using the criteria in Equations (1) and (2), we have obtained a sample of 126,884 LRGs.

For both the BG and LRG samples, we extracted cutouts of 101×101 pixels, corresponding to 20×20 arcsec^2, centered on each of these galaxies from the r-band coadded images from KiDS DR4. The cutout sizes (corresponding to 90 kpc $\times$ 90 kpc at $z = 0.3$ or 120 kpc $\times$ 120 kpc at $z = 0.5$) are large enough to enclose from galaxy-sized to group/cluster-sized arcs and mupols and have a sense of the environment around the lens candidates.

2.2. The Training Data

The training data represent the data set from which the CNN has to learn which features should be detected in the predictive data set to allow the classification. In general, it is composed of "true positives," i.e., real confirmed lens systems, and "true negatives," i.e., systems containing no detectable lensed images but that can contain features similar to the ones of true lensing events that the CNN has to learn to exclude (e.g., blue spiral arms mimicking a lensed arc or ring galaxies mimicking Einstein rings; see a more detailed discussion below). Moreover, the training sample needs to realistically reproduce the data quality of the predictive sample. In case this condition is not fulfilled, and the training sample does not recover the main attributes of a predictive sample, domain adaptation or transfer learning (see e.g., Kouw & Loog 2018) can be applied. This, for instance, will be a necessary approach in the future, when color information will be added to the CNN for the classification.

Since we do not have a large sample of real lenses in KiDS (i.e., most of the candidates from P19 and other papers are not confirmed yet),[15] to build up true positives, we simulated realistic arcs around a selected sample of galaxies extracted randomly from the predictive sample (see, e.g., Petrillo et al. 2017). To this purpose, we followed the description in P19. We used a singular isothermal ellipsoid (SIE) profile plus external shear to model the deflectors and a Sérsic profile to model the

---

light of the background sources. The model parameters have been set as in Petrillo et al. (2019a), where they were demonstrated to be realistic enough. In particular, the Einstein radius was set to be in the range [1″, 5″] and follow a logarithmic distribution. Additionally, the Gaussian random field accounting for the effect of the subhalos of the deflector and small light blocks (modeled with Sérsic profiles) reproducing the corresponding source substructures implemented in P19 were also added. When training the CNN classifier, we rescaled the brightness of the arcs by the peak light of the central galaxies and normalized all images to the same range of counts, [0, 255]. We also did data augmentation for positives (the simulated lenses) and negatives in the training process (e.g., rotation, shifting, flipping, and rescale).

Thus, in summary, the training data have been divided into two classes: the positives and the negatives. The positives are the "true lenses," i.e., galaxies around which we know there is a (simulated) arc, that we labeled with a [1], while negatives are the "no-lens galaxies," i.e., real KiDS galaxies with no simulated arcs, and we labeled them with a [0]. Below, we describe in more detail how these two classes have been constructed.

1. Positives. We have selected 11,000 LRGs from the LRG sample, of which about half were provided by P19 and half were selected by us via visual inspection. We then simulated 200,000 arcs and convolved them with an average PSF of KiDS DR4. For each arc, we randomly chose an LRG from the selected sample and added the arc to it to create a mock lens system. With this method, we built 200,000 mock lenses, suitable to be used as positives to train our CNN.

2. Negatives. This sample is made up of a total of 18,000 real galaxies, comprising the 11,000 LRGs that we used to simulate the positives, 3000 nonlens galaxies randomly selected from KiDS DR4, 2000 spiral galaxies (of which 1000 were provided by P19 and another 1000 were selected by us through visual inspection of KiDS DR4 images) used to train the CNN to avoid false positives produced by spiral arms, and 2000 other kinds of false positives (e.g., mergers, ring galaxies, etc.). In particular, for this latter class, we selected candidates that the CNNs that we built to test the different architectures (see Section 2) classified as probable lenses but that were then rejected after visual inspection.

Figure 1 shows examples of the training sample. The images in the first row show three simulated lenses (positives) by adding mock arcs to real LRGs. In the same figure, the second row shows three real galaxies used as negatives.

Here we stress two points. First, our assumptions do not account for correlations between the lens galaxy properties and the lensed images in the simulating process. Although in real lenses, the galaxy mass and light are correlated, we have made this choice to avoid any possible bias (e.g., assuming a specific dark-to-luminous mass ratio, e.g., from abundance matching; see Moster et al. 2010). Indeed, given the large uncertainties in these relations and the limited mass range of lens galaxies, the adoption of a correlation with realistic variance would have produced an almost uniform bivariate distribution, equivalent to no correlation. Second, our choice to use only LRGs to simulate real lenses in the training sample is meant to optimize the CNN predictive power primarily over this sample, but it
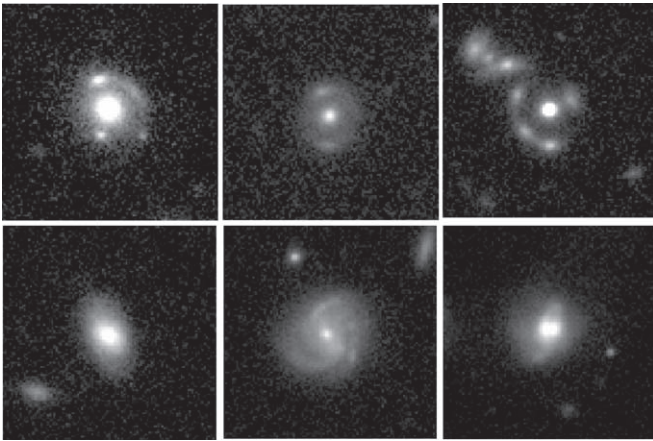
Figure 1. Examples of the training sample. The pictures in the first row are three simulated lenses (positives) produced by adding mock arcs to real LRGs. The pictures in the second row are three real galaxies used as negatives.

might impact the predictive power for the bright sample. We stress, though, that the BGs are not expected to have attributes (e.g., luminosity, size, flattening) that differ significantly from those of the LRGs and that might, in some way, affect the ability of the CNN to discriminate true positives (either arcs or mupols around galaxies; see also Section 3.4). From this point of view, the application of the CNN, trained on the LRGs, to the BGs does not justify the use of transfer learning (see, e.g., Kouw & Loog 2018). In principle, we could have used this approach, in case we had used multiple band information, as color is the only distinctive parameter of the two predictive samples. Since, for the moment, we use only the *r*band, we do not expect this feature to affect the CNN performance or produce overfitting. However, we will investigate the use of transfer learning in the next analyses, when we will compare the results of CNNs trained on the *r*band only and those of CNNs trained on multiband images.

2.3. Testing the CNN Classifier

After training, the CNN classifier was tested on a test sample to evaluate its performance. The test sample was made of 2000 simulated lenses, following the prescription in Section 2.2, as positives and 2000 randomly selected real galaxies from the LRG sample as negatives. We note that we only used galaxies in the LRG sample for testing, since the CNN is trained only on that.

We use the receiver operating characteristic (ROC) curve to evaluate the performance of the CNN classifier (see also Petrillo et al. 2019a). The ROC curve is obtained by plotting the true-positive rate (TPR) against the false-positive rate (FPR) for different p_{CNN} thresholds, where TPR and FPR are defined as follows.

1. TPR: the fraction of positives that have also been identified as positives by the classifier (i.e., objects on which the classifier works properly).
2. FPR: the fraction of negatives that have been wrongly classified as positives by the classifier.

In Figure 2, we show the ROC curve (left) and the probability distribution (right) of the whole testing sample (2000 simulated lenses and 2000 real nonlens galaxies, both

taken from the LRG sample, which is the one we use to train the CNN). The ROC curve is similar to the one in Petrillo et al. (2019a), showing that the two CNNs perform very similarly. In the right panel of the figure, what we plot is the distribution of the output CNN probability of true positives (i.e., lenses, in blue) versus negatives (i.e., nonlenses, in gray). The figure demonstrates that a fraction of real lenses can be lost because they are wrongly rejected by the classifier and assigned a very low probability. We have visually inspected these cases within the testing sample, finding that the majority of missed lenses have arcs that are too faint to be recognized or are embedded in the light of the foreground galaxy. This shows that the current CNN performs well for bright arcs, while for more extreme configurations (e.g., very small Einstein radii), some improvements are still required, which we will implement in the next developments.

The figure also clearly shows that for higher p_{CNN}, the fraction of negatives decreases. Thus, a threshold can be defined to select good candidates. In this paper, we decided to adopt $p_{CNN} = 0.75$, above which the fraction of negatives always remains below 6.5%.

3. New Lens Candidates

The compilation of the lens candidates is based on two steps: the first step is the classification by the CNN, and the second step is the visual inspection by five expert observers. This latter step is necessary to clean the final sample of clear false positives and add an independent score to the lenses for which the CNN has returned a high probability. This allows us to optimize the chance that a given candidate can be a real lens, as this selection process involves both artificial and human intelligence. In future large surveys (e.g., LSST, Euclid, and CSST), the visual inspection by experts will represent a severe bottleneck for the process, as the number of candidates from a CNN classifier will be on the order of several hundred thousand. Hence, human inspection will be doable only through some form of citizen science project (see, e.g., More et al. 2016). In the alternative, we we will need to find other automatic filtering techniques to further prune the candidates from obvious false positives and reduce the sample to visually inspect to reasonable sizes for large collaborations (e.g., of the order of several tens of thousands).

3.1. CNN Probability and Preliminary Candidate Selection

After training and testing the CNN, we first applied the network to make predictions (i.e., look for arcs) on the LRG sample. In this case, the input of the CNN is the set of 126,884 normalized images of the LRG sample described in Section 2.1, while the output is the probability, p_{CNN}, for each of them to be a lens.

As already specified in Section 2.3, we set a threshold probability of $p_{CNN} = 0.75$ to define a system as a valuable lens candidate and qualify for the visual inspection. This threshold has been set as a reasonable trade-off between the CNN probability output of true lenses and a false positive in the training run (see Figure 2). Note that this threshold is different from the one adopted in P19 ($p_{CNN} = 0.8$) but returned a similar number of potential candidates (see the discussion in Section 4).
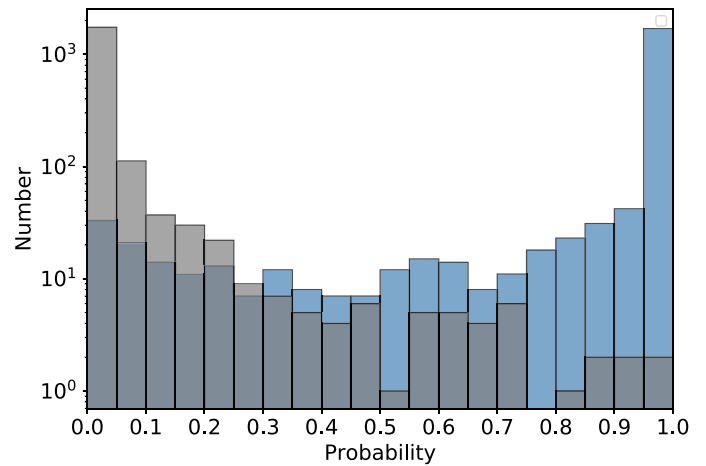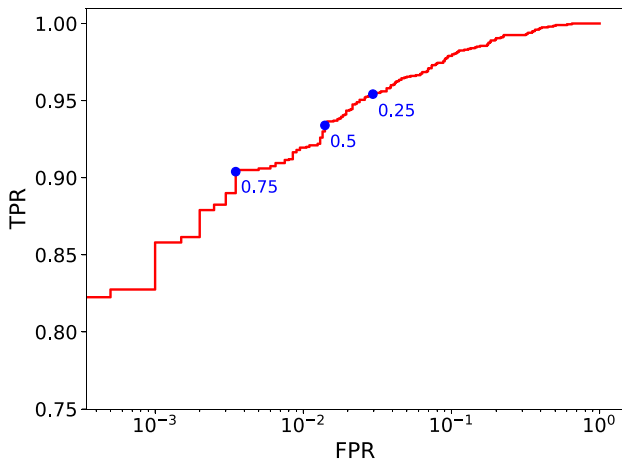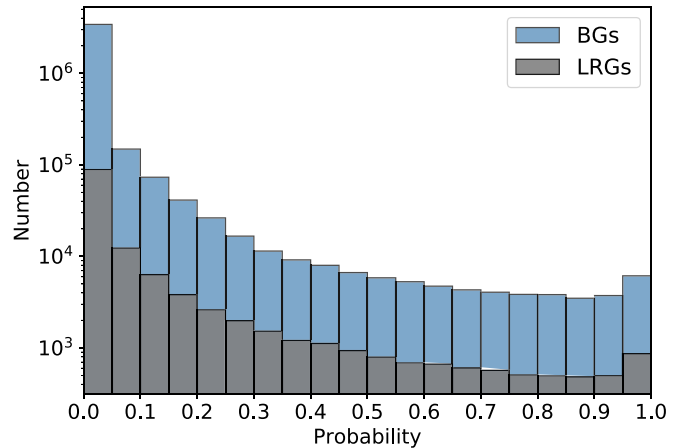
Figure 2. Left: ROC curve for the CNN classifier based on 4000 galaxies in the testing sample. We also show the locations of three different values of the threshold ($p_{CNN} = 0.25$, 0.5, and 0.75) used to calculate the FPR and TPR. Right: probability distribution of the testing sample. The blue histogram represents the probability distribution of the positives, while the gray histogram shows that of the negatives.
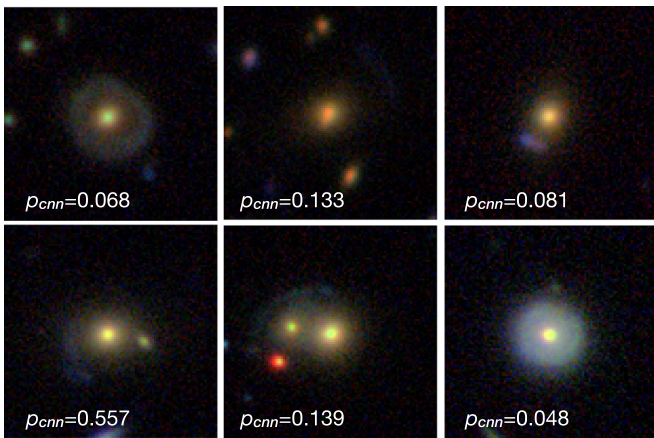
Figure 3. Six lens candidates found by P19 but missed by our CNN. Here p_{CNN} is the probability from our CNN classifier. The stamps ($20'' \times 20''$) are obtained by combining g, r, and i images.

Figure 4. Probability distribution of the predictive LRGs (gray) and BGs (blue). The two distributions follow the logarithm form, which is just as we expected.

We have obtained 2848 candidates (2.24% of the full LRG sample), including 54 of the 60 high-quality LinKS lens candidates already classified by P19, corresponding to a 90.0% recovery rate. The six "missing" objects, whose color-combined KiDS cutouts are shown in Figure 3, have probabilities lower than the threshold we fixed. Some of them might be real lenses missed by our CNN classifier. On the other hand, we find and present here good candidates missed by the CNN of P19. A full comparison of the two classifiers is beyond the purpose of this paper and will be addressed in detail in a forthcoming work. Here we note that, despite the similarities between the two classifiers, they are not identical (see the summary of the differences between them in Section 4), and, as such, they present interesting complementary aspects. This demonstrates the importance of developing independent ML classifiers (either CNNs or other ML techniques, such as support vector machines (SVMs), etc.), and possibly exploiting the combined strengths of each of them to further improve the overall performances of hybrid configurations.

We have then applied our CNN model to the full BG sample, which is, however, more prone to induce a larger number of false positives, since the CNN is not optimized for this sample.

Moreover, the BG sample also includes slightly fainter galaxies with any color, thus also late-type systems, whose spirals could mimic arc-like lensing features. In order to reduce the fraction of such false positives, in this case, we have set a higher (and quite conservative) probability threshold to $p_{CNN} = 0.98$ to accept a system as a valuable lens candidate. With this threshold, we have obtained 3552 lens candidates, corresponding to 0.093% of the BG sample.

In Figure 4, we show the distributions of the CNN probability of the LRG and BG samples. Overall, the two distributions follow a characteristic logarithmic trend, which is scaled according to the relative sample sizes. This trend is as expected, because targets with smaller CNN probabilities tend to be no-lens, while those with larger probabilities tend to be real lenses, and there are far more no-lenses in the real predictive samples compared to lenses.

3.2. Visual Inspection

Both lists of candidates (from the LRG and BG samples) are definitely larger than the number of real lenses one can expect in the covered area ($\sim$500 in 1000 deg^2; Collett 2015), which
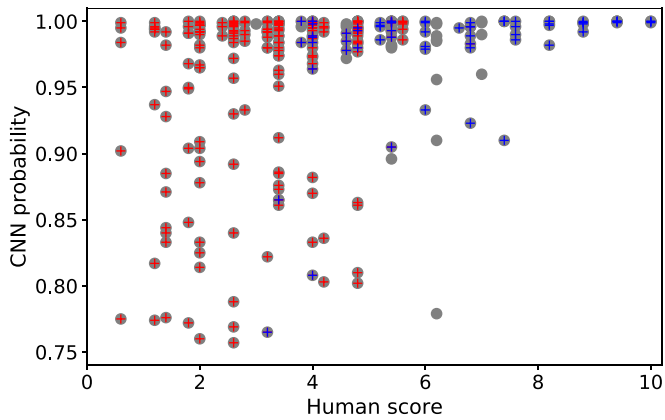
Figure 5. CNN probability p_{CNN} against human probability p_{hum} for the 286 new candidates that passed both the ML and human thresholds. Points marked with blue plus signs represent the systems for which at least one inspector gave a score of 10 (i.e., sure lens), while points marked with red plus signs represent the systems for which at least one inspector gave a score equal to zero (i.e., not a lens).

means that these samples are dominated by false positives. In order to optimize the next visual inspection step and give more time to inspectors to concentrate on significant candidates, we decided to have a first pass to filter clear false positives. In this case, only one observer had the task of inspecting all candidates (2848 from LRG sample plus 3552 from the BG sample) and excluded obvious nonlenses from the final sample to inspect. In this preliminary phase, we have also excluded all of the lens candidates found by the CNN from P19 and Petrillo et al. (2017), including the LinKS sample, bonus sample, and any others they mentioned. The final number of candidates that survived this process was 286,133 from the LRG sample and 153 from the BG sample.

The next step was to let five observers inspect the objects selected on the basis of the CNN probability that passed the visual preselection "cleaning." To this purpose, we created a color cutout of $20'' \times 20''$ combining the g, r, and i bands and let five people inspect the sample of 286 preselected objects in a blind way. The inspectors had to assign to each system a quality letter following an *ABCD* scheme, where *A* is surely a lens, *B* is maybe a lens, *C* is maybe not a lens, and *D* is not a lens, which we associated with marks of 10, 7, 3, and 0, respectively, to convert the quality flags into a score.

We stress here that visual inspection does not provide proof that a candidate lens is real. In this respect, until we have access to a statistically large sample of spectroscopically confirmed lenses in KiDS, ML will reproduce the human bias to define a lens as real. The best way to reduce this bias is indeed to increase the number of independent team members performing the visual assessment of the CNN lenses, as already stated in P19. This is why in this paper, we always use five different inspectors to grade the candidates.

Finally, we defined a human probability as $p_{hum} = s_{ave}/10$, where s_{ave} is the average score from five inspectors. This human scoring returned 18 candidates with very high probability ($p_{hum} \geqslant 0.8$) and another 10 with slightly lower probabilities ($0.7 \leqslant p_{hum} \leqslant 0.8$) but still very convincing. These objects also all received very high values from the CNN, as can be seen in Figure 5. In this figure, we plot the CNN probability p_{CNN} versus the human probability p_{hum}. The 28

candidates are located in the top right corner of the plot; they have received high probabilities from both CNN and humans.

Moving toward lower p_{hum}, in the plot, one should also expect p_{CNN} to decrease, and ideally, the two quantities should be correlated. Instead, there is no clear correlation between p_{CNN} and p_{hum}, as the CNN also gives a higher significance to candidates that are poorly ranked by humans, although we observe a clear increase in the scatter between the two quantities. In the upper left corner of Figure 5, there are systems with very high $p_{CNN}(\geqslant 0.97)$ but very low $p_{hum}(\leqslant 0.4)$. In these cases, the CNN either performs better than human eyes to detect real features that are not recognized by the inspectors or more easily confuses features that can mimic gravitational arcs and mupols, which are more likely considered false positives from humans. Figure 6 clearly demonstrates that the latter option is more likely the case. We show here a few cases of candidates with high p_{CNN} ($\geqslant 0.97$) and low p_{hum} ($=0.2$). Most of them are likely to be false positives, since they show features (interactions, spiral arms, rings, etc.) that mimic both faint arcs and mupols. This suggests that further effort is needed to improve the training set by including more accurate negatives. However, for these systems, we cannot rule out the possibility that small Einstein-radius lenses can be found by the CNN but are harder to see by the inspectors, since the lensed images are hidden in the light of the central galaxies. But this problem can be partly overcome in the future by removing the light of the foreground galaxies.

In the middle region of Figure 5, there are candidates for which the inspectors did not unanimously agree on the classification, and thus the final human probabilities are in the range of $0.4 \leqslant p_{CNN} \leqslant 0.6$. Here a large scatter in the CNN probability is found, probably because the machine tends to pick some features that have a lower signal-to-noise ratio (S/N) and are considered not totally convincing for humans.

In order to figure how plausible the high p_{CNN} can be in this range of p_{hum}, we marked all of the points in Figure 5 for which at least one inspector considered the system a sure lens (i.e., gave a grade of 10) with blue plus signs. Many of these systems turned out to be mupols. This might indicate that the CNN has to be improved in the selection of this particular category of lenses. We expect to better qualify these candidates with forthcoming experiments, training the CNN on this specific class of systems. We note that red plus signs indicate systems for which at least one inspector gave a score = 0 (i.e., considered that object a clear contaminant).

3.3. Ranking the Candidates

Overall, Figure 5 suggests that neither the p_{CNN} nor the p_{hum} are, alone, fully suitable parameters to rank the lenses (note that this is true for the current CNN but might not be true for better networks). Hence, we decided to combine the two quantities to find a compromise between the CNN and human "predictions" and adopt a pseudo- (joint) probability as a metric to rank the candidates:

$$\mathbb{P} = p_{CNN} * p_{hum}. \tag{3}$$

Using this probability, we identify 82 candidates with a *P*-value $\geqslant 0.5$, which we define as high-quality lens candidates. Among them, 26 candidates represent a "golden" sample with a *P*-value $\geqslant 0.7$, all showing obvious lens features and thus very suitable for spectroscopic follow-up observations.
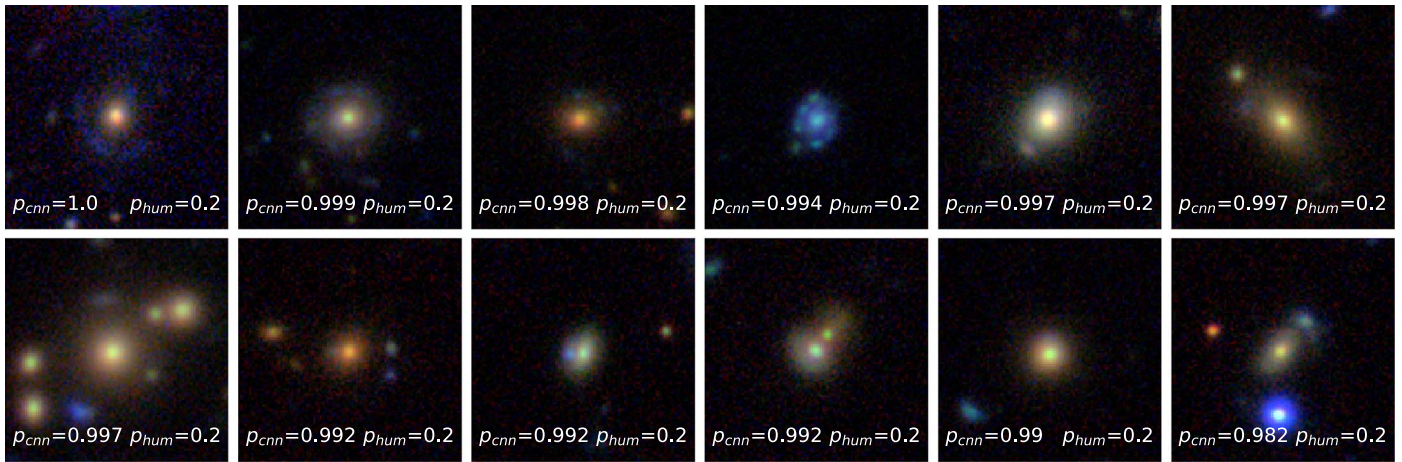
Figure 6. Candidates with high CNN probability ($p_{\mathrm{CNN}} \geqslant 0.97$) and low human score ($p_{\mathrm{hum}} = 0.2$). There are some arc-like but nonlens features (interactions, spiral arms, rings, etc.) that can give rise to some high values of p_{CNN}.

In Table 1, we report the lens ID, KiDS name, coordinates, r-band magnitude, photometric redshift, average score s_{ave} from the inspectors, p_{CNN}, and P-values of the 82 high-quality candidates, ranked in order of decreasing P-value. Finally, in the last column of the table, we report the number of inspectors that gave a zero score to that particular object. In fact, as we described at the beginning of Section 3.2, a first prefiltering of the 6400 objects with a p_{CNN} higher than the threshold was made by one single inspector. This person excluded obvious nonlenses from the final sample of candidates (286) that were then passed to four other people. This can be interpreted as assigning a zero score to the excluded objects. Thus, formally, we should now exclude all systems where at least one of the remaining inspectors gave a zero score. In this case, we would get rid of most of the low scores and lower p_{cnn} in Figure 5 (in the bottom left region of the plot), where we mark with red plus signs systems that received at least one zero score. However, at the same time, we would also exclude many objects that received a very high grade from the CNN and could still be reliable candidates. We therefore decided to keep and flag these systems, since, as already stressed, we have no way to understand if visual inspection works better/worse than the CNN. We thus believe that reporting the number of inspectors that gave a zero in Table 1 and the stamps we show in Figure 8 is the best way to let readers judge for themselves.

3.4. The High-quality Lens Sample

The 82 high-quality candidates, ranked in order of decreasing P-value, are shown in Figure 8. The stamps ($20'' \times 20''$) are obtained by combining g-, r-, and i-band images. We stress that the intrinsic S/N can change quite a lot in the different bands, since the g and i bands have worse seeing and depth with respect to the r band. This might also be a factor of discrepancy between the CNN and human score, since the former only uses the r band, while the visual inspection is made on the color-combined images and could be driven more by the combined S/N. We will expand the CNN predictions to other bands in forthcoming analyses (see also the first attempt of this kind in Petrillo et al. 2019b, 2019a). We stress that this implementation needs very accurate color information when building the training sample. The color distribution of the sources has to reproduce the realistic colors of real galaxies, otherwise its

usage can lead to contradictory results. For instance, Metcalf et al. (2019) showed that, for their testing sample, multicolor data are powerful in the lensing search, as multiband ground-based data can reach better performance when compared with single-band space-based data with lower noise and higher resolution. However, Petrillo et al. (2019a) also found that the color information can only partially help to improve the predictive ability of the CNN, since the CNN is mostly driven by morphology. The addition of color information might become troublesome if the lens colors are heavily contaminated by the colors of the sources (i.e., looking bluer that they truly are, e.g., because of the close presence of very bright quasars). Thus, a very careful identification of proper color cuts and a proper training sample, reproducing the variety of colors and magnitudes of real lenses, are needed to make the multiband approach effective.

At first glance, the majority of the candidates show distinguishable arc-like features, but some mupols candidates are also present. These candidates increase the number of previously found lensed quasar candidates in KiDS using information from source colors in the optical and infrared (see, e.g., Spiniello et al. 2018; Khramtsov et al. 2019; Petrillo et al. 2019b). In particular, ID = 1 shows a very convincing peculiar Einstein cross-configuration, while ID = 12 seems to be a classical quadruplet in a fold configuration. Also, ID = 5 is likely a quad, with broad peaks due to the worse i-band seeing that will be dominant, given the peculiar red color of the arc. These objects are definitely very interesting for spectroscopic follow-up, as, if confirmed, they will increase the number of know quads that are particularly useful for monitoring campaigns aimed at accurate measurements of the Hubble constant (H_0; Suyu et al. 2017; Wong et al. 2020).

Another important note is that about half of the candidates in the golden sample are found in the BG sample (e.g., ID = 3, 7, 10, 12, 13, 15, 16, 17, 18, 19, 20), which demonstrates that the ability of the CNN to find arcs and mupols around these systems has not been particularly affected by the training sample based on LRGs only (see Section 2.2).

Finally, the CNN has captured some larger Einstein radii from groups/clusters like ID = 7, which shows a very faint and very red central deflector but a relatively large Einstein radius ($\sim 5''$), with three arc-like images on the left and one

Table 1
Properties of the Best 82 Lens Candidates

ID	KiDS_NAME	R.A. J2000	Decl. J2000	r_{auto}	z_{phot}	s_{ave}	rms	p_{cnn}	P-value	No. Zero Scores
1	KiDS J122456.016+005048.05	186.233401	0.846682	17.96	$0.43^{+0.02}_{-0.04}$	10.0	0.0	1.0	1.0	0
2	KiDS J111253.976+001044.65	168.224904	0.179072	18.26	$0.49^{+0.02}_{-0.03}$	10.0	0.0	1.0	1.0	0
3	KiDS J233533.673−322722.06	353.890307	−32.456128	19.59	$0.67^{+0.02}_{-0.03}$	10.0	0.0	0.999	0.999	0
4	KiDS J013425.700−295652.42	23.607086	−29.947897	18.73	$0.59^{+0.02}_{-0.04}$	9.4	1.2	1.0	0.94	0
5	KiDS J083933.372−014044.81	129.889052	−1.679115	17.17	$0.62^{+0.02}_{-0.04}$	9.4	1.2	1.0	0.94	0
6	KiDS J134032.074−003737.83	205.133643	−0.627175	18.05	$0.4^{+0.02}_{-0.04}$	9.4	1.2	1.0	0.94	0
7	KiDS J010704.918−312841.03	16.770493	−31.478064	20.25	$0.86^{+0.02}_{-0.03}$	9.4	1.2	1.0	0.94	0
8	KiDS J024228.926−294305.41	40.620528	−29.718171	19.42	$0.51^{+0.02}_{-0.03}$	9.4	1.2	0.999	0.939	0
9	KiDS J123554.179+005550.41	188.97575	0.93067	18.49	$0.43^{+0.02}_{-0.04}$	8.8	1.47	1.0	0.88	0
10	KiDS J010606.232−310437.84	16.525969	−31.07718	17.98	$0.7^{+0.03}_{-0.03}$	8.8	1.47	0.999	0.879	0
11	KiDS J235728.351−352013.03	359.368133	−35.336955	17.27	$0.7^{+0.02}_{-0.03}$	8.8	1.47	0.999	0.879	0
12	KiDS J104223.359+001521.24	160.59733	0.2559	20.0	$0.75^{+0.03}_{-0.03}$	8.8	1.47	0.998	0.878	0
13	KiDS J231242.301−332318.44	348.176257	−33.388457	19.83	$0.69^{+0.02}_{-0.04}$	8.8	1.47	0.992	0.873	0
14	KiDS J021504.013−284248.57	33.766723	−28.713492	18.59	$0.45^{+0.02}_{-0.03}$	8.2	1.47	1.0	0.82	0
15	KiDS J090507.336−001029.85	136.28057	−0.17496	19.59	$0.71^{+0.02}_{-0.04}$	8.2	1.47	1.0	0.82	0
16	KiDS J025334.181−284611.92	43.392423	−28.769978	19.82	$0.64^{+0.02}_{-0.04}$	8.2	1.47	0.998	0.818	0
17	KiDS J003151.142−312638.83	7.963094	−31.44412	19.74	$0.65^{+0.02}_{-0.04}$	8.2	1.47	0.997	0.818	0
18	KiDS J005540.416−290042.46	13.918401	−29.011797	18.41	$0.25^{+0.02}_{-0.03}$	8.2	1.47	0.982	0.805	0
19	KiDS J010257.486−291121.76	15.739527	−29.189379	17.39	$0.39^{+0.02}_{-0.03}$	7.6	1.2	1.0	0.76	0
20	KiDS J112900.041−014214.01	172.250173	−1.703894	19.89	$0.69^{+0.02}_{-0.04}$	7.6	1.2	0.996	0.757	0
21	KiDS J233620.351−352555.55	354.084799	−35.4321	19.52	$0.51^{+0.02}_{-0.04}$	7.6	1.2	0.99	0.752	0
22	KiDS J232152.835−275437.68	350.47015	−27.910469	19.65	$0.69^{+0.02}_{-0.03}$	7.6	1.2	0.986	0.749	0
23	KiDS J100108.387+024029.67	150.284948	2.67491	19.51	$0.32^{+0.03}_{-0.03}$	7.4	2.58	1.0	0.74	0
24	KiDS J234338.567−335641.44	355.910697	−33.944845	18.24	$0.32^{+0.02}_{-0.03}$	7.4	2.58	1.0	0.74	0
25	KiDS J125834.900−004241.11	194.645418	−0.711421	16.78	$0.27^{+0.02}_{-0.03}$	7.4	2.58	1.0	0.74	0
26	KiDS J014518.788−290539.92	26.328284	−29.094423	19.29	$0.51^{+0.03}_{-0.03}$	7.0	0.0	1.0	0.7	0
27	KiDS J112152.078+023711.11	170.466993	2.619754	19.9	$0.55^{+0.02}_{-0.04}$	7.0	0.0	0.999	0.699	0
28	KiDS J000820.374−342718.99	2.084894	−34.455275	19.16	$0.42^{+0.02}_{-0.03}$	7.0	0.0	0.99	0.693	0
29	KiDS J224258.953−351223.13	340.74564	−35.206425	17.92	$0.66^{+0.02}_{-0.04}$	6.8	2.23	0.999	0.679	0
30	KiDS J133317.497+005907.56	203.322906	0.985436	18.72	$0.32^{+0.02}_{-0.03}$	6.8	2.23	0.996	0.677	0
31	KiDS J154712.516+002809.44	236.80215	0.469289	19.22	$0.44^{+0.02}_{-0.03}$	6.8	3.65	0.996	0.677	1
32	KiDS J000517.478−352342.48	1.322827	−35.395134	19.41	$0.59^{+0.03}_{-0.04}$	6.8	2.23	0.996	0.677	0
33	KiDS J023714.701−280719.03	39.311257	−28.121953	17.62	$0.56^{+0.03}_{-0.04}$	7.4	2.58	0.91	0.673	0
34	KiDS J235920.307−290744.83	359.834614	−29.129122	18.79	$0.34^{+0.08}_{-0.04}$	6.8	2.23	0.989	0.673	0
35	KiDS J225409.348−274934.16	343.538954	−27.826156	18.45	$0.46^{+0.02}_{-0.04}$	7.0	0.0	0.96	0.672	0
36	KiDS J022956.259−311022.65	37.484416	−31.172959	20.78	$0.56^{+0.03}_{-0.04}$	6.8	3.65	0.983	0.668	1
37	KiDS J030628.054−291718.77	46.616892	−29.288548	18.61	$0.27^{+0.02}_{-0.04}$	6.8	2.23	0.98	0.666	0
38	KiDS J144950.559+005534.07	222.460665	0.926133	19.39	$0.76^{+0.02}_{-0.03}$	6.6	3.14	0.995	0.657	0
39	KiDS J032230.223−344711.77	50.625931	−34.786604	19.2	$0.45^{+0.02}_{-0.03}$	6.8	2.23	0.923	0.628	0
40	KiDS J232911.441−324256.22	352.297671	−32.715617	19.45	$0.42^{+0.02}_{-0.04}$	6.2	1.6	0.998	0.619	0
41	KiDS J002105.099−283818.44	5.271248	−28.638458	18.88	$0.46^{+0.02}_{-0.04}$	6.2	1.6	0.999	0.619	0
42	KiDS J232039.461−281711.12	350.164421	−28.286423	18.63	$0.5^{+0.03}_{-0.03}$	6.2	1.6	0.989	0.613	0
43	KiDS J231310.384−344646.65	348.293267	−34.779625	18.31	$0.29^{+0.02}_{-0.03}$	6.2	1.6	0.985	0.611	0
44	KiDS J004439.128−291957.30	11.163036	−29.332586	17.52	$0.31^{+0.02}_{-0.03}$	6.2	1.6	0.986	0.611	0
45	KiDS J011731.429−314432.70	19.380956	−31.742419	19.75	$0.6^{+0.03}_{-0.03}$	6.0	2.68	1.0	0.6	0
46	KiDS J010649.164−284137.90	16.704852	−28.693863	17.93	$0.59^{+0.02}_{-0.04}$	6.0	2.68	0.999	0.599	0
47	KiDS J125814.219−005013.87	194.55925	−0.837188	19.68	$0.64^{+0.02}_{-0.04}$	6.0	2.68	0.992	0.595	0
48	KiDS J145325.778−003331.75	223.357411	−0.558822	19.22	$0.59^{+0.02}_{-0.04}$	6.2	1.6	0.956	0.593	0
49	KiDS J031142.084−341928.80	47.925354	−34.324669	18.72	$0.45^{+0.02}_{-0.04}$	6.0	2.68	0.981	0.589	0
50	KiDS J020554.272−342019.30	31.476136	−34.338695	18.11	$0.42^{+0.02}_{-0.04}$	6.0	2.68	0.979	0.587	0
51	KiDS J141913.862+025635.41	214.807762	2.94317	18.86	$0.42^{+0.02}_{-0.04}$	6.2	1.6	0.91	0.564	0
52	KiDS J115110.395+025642.08	177.793313	2.945024	17.82	$0.43^{+0.02}_{-0.03}$	6.0	2.68	0.933	0.56	0
53	KiDS J004558.739−331451.79	11.494746	−33.24772	19.18	$0.47^{+0.02}_{-0.03}$	5.6	2.8	1.0	0.56	1
54	KiDS J015928.393−330950.36	29.868305	−33.16399	19.35	$0.46^{+0.02}_{-0.04}$	5.6	2.8	1.0	0.56	1
55	KiDS J224712.244−333827.77	341.801017	−33.641048	17.94	$0.33^{+0.02}_{-0.04}$	5.6	2.8	0.999	0.559	1
56	KiDS J235255.478−291728.16	358.23116	−29.291158	18.71	$0.47^{+0.02}_{-0.03}$	5.6	2.8	0.998	0.559	1
57	KiDS J135138.926+002839.99	207.912195	0.477777	19.36	$0.58^{+0.03}_{-0.03}$	5.6	2.8	0.994	0.557	1
58	KiDS J021609.168−293550.74	34.0382	−29.597429	20.28	$0.75^{+0.02}_{-0.03}$	5.6	2.8	0.986	0.552	1

Table 1
(Continued)

ID	KiDS_NAME	R.A. J2000	Decl. J2000	r_{auto}	z_{phot}	s_{ave}	rms	p_{cnn}	P-value	No. Zero Scores
59	KiDS J224308.305−344213.02	340.784606	−34.703619	19.09	$0.39^{+0.03}_{-0.04}$	5.4	1.96	1.0	0.54	0
60	KiDS J121234.927+000754.48	183.145531	0.1318	16.73	$0.25^{+0.02}_{-0.03}$	5.4	3.5	1.0	0.54	1
61	KiDS J021555.605−342425.72	33.98169	−34.407147	19.3	$0.54^{+0.04}_{-0.04}$	5.4	1.96	1.0	0.54	0
62	KiDS J235510.007−283212.34	358.791698	−28.536762	16.24	$0.28^{+0.02}_{-0.03}$	5.4	1.96	1.0	0.54	0
63	KiDS J000012.031−310943.35	0.050133	−31.162044	19.11	$0.42^{+0.03}_{-0.03}$	5.4	3.5	1.0	0.54	1
64	KiDS J230527.508−313700.76	346.364619	−31.61688	18.59	$0.32^{+0.02}_{-0.03}$	5.4	1.96	1.0	0.54	0
65	KiDS J031516.618−310754.18	48.819245	−31.131718	17.96	$0.49^{+0.02}_{-0.03}$	5.4	3.5	0.999	0.539	1
66	KiDS J091113.492−000714.23	137.80622	−0.12062	17.88	$0.37^{+0.03}_{-0.03}$	5.4	1.96	0.999	0.539	0
67	KiDS J134455.641−002015.60	206.231838	−0.337667	18.87	$0.45^{+0.02}_{-0.03}$	5.4	1.96	0.998	0.539	0
68	KiDS J223123.786−282504.50	337.849109	−28.417917	18.51	$0.37^{+0.02}_{-0.03}$	5.4	3.5	0.999	0.539	1
69	KiDS J121319.575+014736.02	183.331564	1.793341	17.63	$0.27^{+0.02}_{-0.03}$	5.4	1.96	0.994	0.537	0
70	KiDS J011045.486−290822.53	17.689526	−29.139593	18.17	$0.34^{+0.02}_{-0.03}$	5.4	1.96	0.994	0.537	0
71	KiDS J003242.839−310335.44	8.178496	−31.059847	19.32	$0.58^{+0.03}_{-0.03}$	5.4	1.96	0.995	0.537	0
72	KiDS J032426.994−290534.50	51.112476	−29.092917	17.92	$0.31^{+0.02}_{-0.03}$	5.4	1.96	0.993	0.536	0
73	KiDS J154051.806+010640.91	235.21586	1.111366	17.31	$0.29^{+0.02}_{-0.03}$	5.4	1.96	0.992	0.536	0
74	KiDS J031609.185−340302.43	49.038271	−34.050677	19.65	$0.56^{+0.03}_{-0.04}$	5.4	3.5	0.993	0.536	1
75	KiDS J221400.330−292031.21	333.501378	−29.342005	20.3	$0.73^{+0.03}_{-0.04}$	5.4	3.5	0.988	0.534	1
76	KiDS J121314.238−001434.63	183.309326	−0.242953	18.58	$0.46^{+0.02}_{-0.04}$	5.4	1.96	0.982	0.53	0
77	KiDS J002141.664−301029.70	5.423603	−30.174917	19.88	$0.67^{+0.02}_{-0.04}$	5.4	1.96	0.981	0.53	0
78	KiDS J122335.140−021030.63	185.896418	−2.175176	18.32	$0.49^{+0.02}_{-0.03}$	5.4	1.96	0.98	0.529	0
79	KiDS J130115.900+025240.95	195.316253	2.878043	18.29	$0.27^{+0.03}_{-0.03}$	5.2	2.86	0.999	0.519	0
80	KiDS J001810.363−285609.54	4.54318	−28.935984	18.84	$0.48^{+0.03}_{-0.03}$	5.2	2.86	0.997	0.518	0
81	KiDS J025717.233−271712.02	44.321807	−27.286673	19.35	$0.59^{+0.02}_{-0.03}$	5.2	2.86	0.996	0.518	0
82	KiDS J104119.501−000416.30	160.331257	−0.071195	19.34	$0.67^{+0.02}_{-0.04}$	5.2	2.86	0.986	0.513	0

Note.—Columns 1–4 list the ID, KiDS name, and coordinates (in degrees) of the candidates, respectively. Column 5 lists the total magnitudes (r_{auto}) obtained from SExtractor. Column 6 lists the photometric redshifts (z_{phot}) taken from the KiDS catalog using the BPZ code. Columns 7 and 8 list the average scores from human inspection and the corresponding rms. Column 9 lists the probability of being a lens from the CNN. Column 10 combines this information into the P-value threshold criterion defined in this work ($P = s_{ave} \times p_{cnn}/10$). Column 11 shows the numbers of inspectors that gave a zero score to that particular candidate (see text for more details).

pointlike image on the right. The deflector has a high photo-z ($z_{phot} = 0.86$, the highest in the candidate list), which is coherent with the red color and the compact size. This is likely to be a dark matter–rich system with one of the largest arc separations from an individual galaxy, especially considering the high redshift of the deflector. However, we cannot exclude the possibility that this system is a galaxy group, since there at least three reddish objects in the vicinity of the lens galaxy candidate. If their redshifts are comparable with that of the central object, then this could be a lensing event from a small group, in this way justifying the larger Einstein radii. We have checked the photometric redshifts, and this does not look to be the case. However, we stress that the photometric redshifts are not always accurate.

The majority of the remaining high-graded systems show quite regular arcs and pseudo-Einstein rings, like ID = 25, 30, 33, 40, and 47.
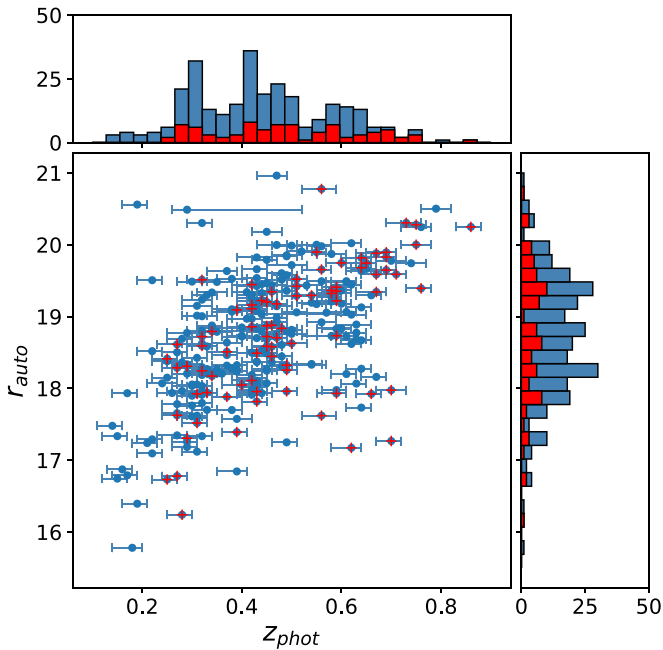
In Figure 7, we show the distribution of the deflectors in the photometric redshift–luminosity space. Photometric redshifts (z_{phot}) are taken from the KiDS catalog and have been obtained using BPZ (for details, please see Kuijken et al. 2019). A correlation between the two quantities is clearly visible, as expected, since, at fixed intrinsic luminosity (we remind the reader that we preselected BGs only), the further a galaxy is (i.e., higher z_{phot}), the smaller the apparent luminosity. The correlation and overall distribution in redshift and luminosity do not change if we include only the candidates in the top 82 ranking (marked

by red plus signs). The photo-z distribution is quite large in redshift and goes from ∼0.2 to ∼0.8. In addition, no correlation between the z_{phot} and the P-value is found, as, for example, we have lenses with redshift ∼0.2 and ∼0.8 among the first 12 ranked candidates, and similarly in the second dozen in the ranking. In general, the redshift distribution of the new lens candidates seems slightly larger than the ones from P19 that have almost no lenses above $z \sim 0.6$.

4. Discussion

The main aim of this paper is to report newly discovered, high-confidence, strong lens candidates in the KiDS DR4. These candidates have been found by applying a CNN classifier that we recently developed following the prescription by P19.

The first question one might ask is: what is the difference between the candidates from the two trained CNNs? The architecture and depth of the network of the CNN we employ in this paper are identical to that of P19. Hence, the difference in the number of candidates mainly comes from the fact that here we expand both the predictive and the training samples. The second question is whether the complementarity of the two approaches can achieve the best completeness of the population of observable gravitational lens candidates. Finally, a third question is whether the number density of these lenses matches with expectations from simple statistical models (e.g., Oguri & Marshall 2010;

Figure 7. Distribution of the 286 lens candidates in the photometric redshift–luminosity space of the foreground deflectors. The dots marked by red plus signs are the first 82 candidates shown in Figure 8. The error bars on the r_{auto} magnitudes are smaller than the symbol sizes.

Collett 2015). This latter question is definitely relevant but beyond the purpose of this paper, as giving an answer would require a deeper analysis of the results coming from different methods. Possibly, this answer can come from an appropriate challenge comparing more techniques (not only the ones developed from our group) that should be run on the same (simulated) data set, using different types of training samples or on different (real) predictive samples in order to establish whether there is an optimal combination of methodologies to obtain the maximum possible completeness.

For the purposes of the current paper, we are limited here to discussing four basic differences between the new CNN and the one from P19. The first difference is the area coverage; in P19, they missed ∼100 tiles that have been made available for the final release, and they removed the masked regions (∼100–200 deg^2) by setting ima_flags = 0 in all four KiDS bands (u, g, i, and r). In this work, we used all 1006 publicly available tiles and did not remove the masked regions. The second difference comes from the number of bands adopted; we used the r band only, while P19 tested both one band (r) and three bands (g, i, and r). This does not necessarily impact the performance of our new CNN. In fact, the seeing in the g and i bands is in many cases worse than that in r-band images. This could reduce the P-value returned by the three-band CNN. A third relevant difference is the training sample. In fact, with respect to P19, we extended the number of LRGs that we used to simulate real lenses, adding simulated arcs to them (positives). Moreover, we also used ∼7000 more nonlensed galaxies to teach the CNN to exclude contaminants (see Section 2.2). On the other hand, we decided to only simulate 200,000 mock lenses to train the CNN, while P19 simulated 1,000,000. We did that because we checked that the addition of more mock lenses would not add more predictive power to the CNN. The fourth difference is the data set adopted to extract

the predictive sample; P19 applied the CNN to KiDS DR4 prepublished data, while we have used the sample qualified for the ESO data release. As already mentioned, these two different data sets have different photometry parameters available (in the ESO DR4, the Kron-like magnitudes are available only for the r band). This resulted in a different LRG sample (our selection included ∼126,000 galaxies, while P19 used ∼88,000), mainly due to a different color definition (despite the same cuts adopted). In P19, the colors are computed from the different bands mag_auto, while we use the COLOUR_GAAP columns given in the multiband catalog and computed from MAG_GAAP magnitudes instead.

This very qualitative comparison does not give a measure of the relative performances of the two CNNs but possibly reveals their complementarity. As mentioned earlier, a full comparison of the performances of the two networks is beyond the purposes of this paper, and we will discuss the differences in their detected systems in a future work.

Other future developments will be oriented toward implementing the completeness of the classifier and reducing the contamination from false positives. For instance, in Section 2.1 we anticipated that a first implementation will consist of the training of the CNN classifier with g, r, and i color-composite images. We also plan to apply both the one- and three-band image-trained CNNs to the future KiDS DR5, where we expect to substantially increase the number of final high-quality candidates in KiDS, since the total covered area will increase by ∼30%.

In the future, our CNN will be easily adapted to the LSST, as both the pixel scale (0.″2 pixel^{-1}) and seeing (<0.″8) are very similar to those of KiDS. We will train the CNN on a simulated sample of lensed arcs and quasars built on LSST-like images (e.g., mock observations) in preparation for running the CNN on real LSST images to find real candidates. According to lens forecasts on LSST, we expect to collect 10^5 lenses at the end of the full depth survey. In this respect, we expect to give a contribution to the ongoing effort to build the necessary machinery to get the completeness of the real lens search close to 100%. Apart from applying our CNN to LSST data, we also plan to apply the CNN to CSST and Euclid, which will provide, from space, much better image quality, and we expect to find ∼10^5 new strong lenses.

5. Conclusions

We have developed a new CNN classifier to search for strong lens candidates in the KiDS DR4 based on the prescription from a former CNN applied to the same KiDS DR4 by P19. The new CNN makes use of independent codes (for both the network and the simulated arcs) and different training and predictive samples. When applied to a sample of LRGs, as done in P19, the new CNN classifier found 90% of the high-quality candidates already presented in P19 (including 10 new "golden" lenses, ID = 1, 2, 4, 5, 6, 8, 9, 11, 14, and 21; see also below). Moreover, by applying this CNN classifier to the whole predictive data set (not only the LRG but also the BG sample without any color cut applied) and combining this with human visual inspection, we found a total of 286 new lens candidates, including arcs, complete rings, and multiple lensed images (e.g., Einstein crosses and quadruplets). We ranked the candidates by combining the CNN probability and the visual score $P = p_{CNN} * p_{hum}$, presented the parameters in Table 1, and show the color-combined cutouts in Figure 8 for the first 82
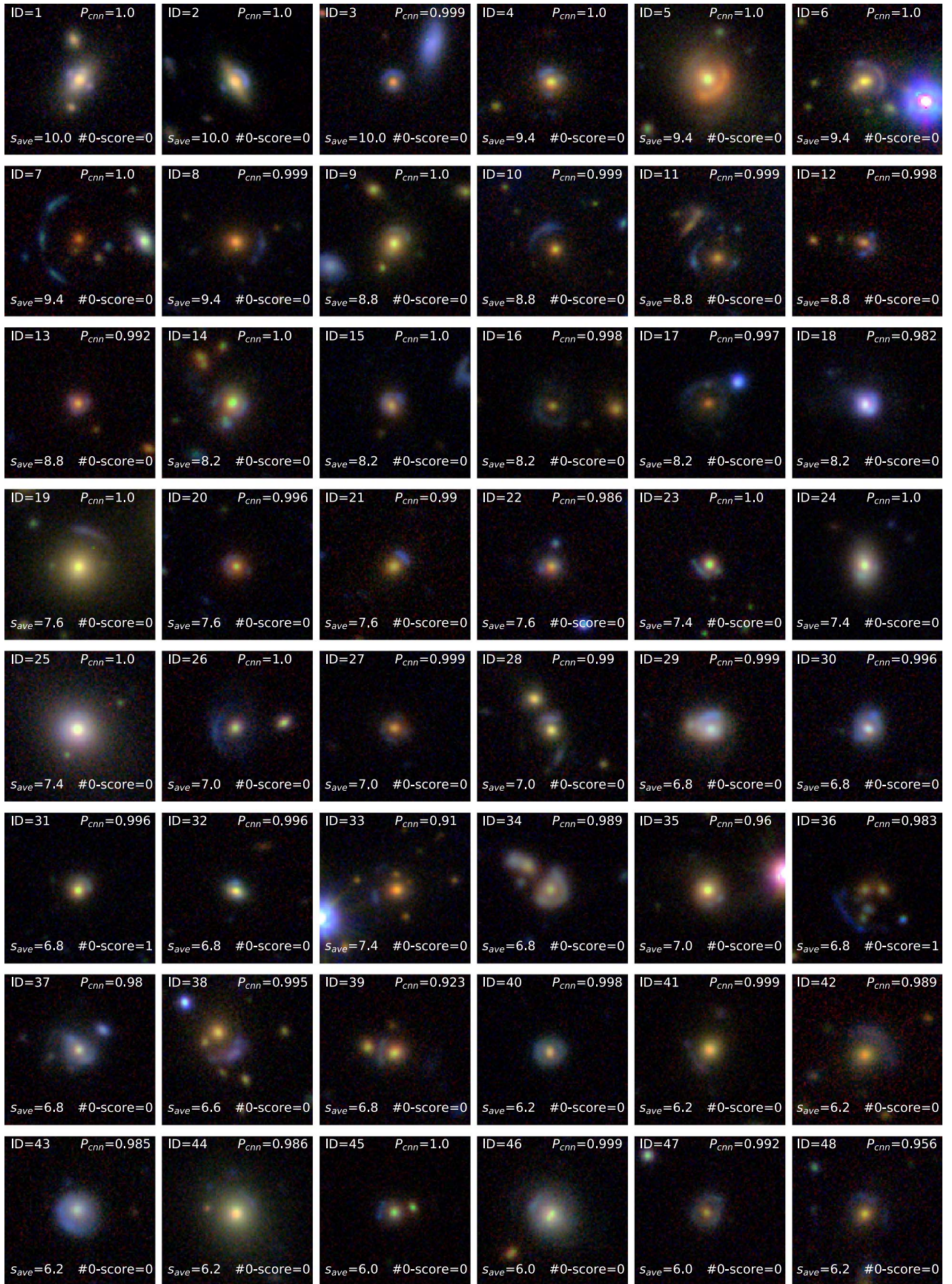
Figure 8. Colored stamps of the 82 best candidates, ranked according to P-value. The stamps ($20'' \times 20''$) are obtained by combining g, r, and i KiDS images.

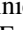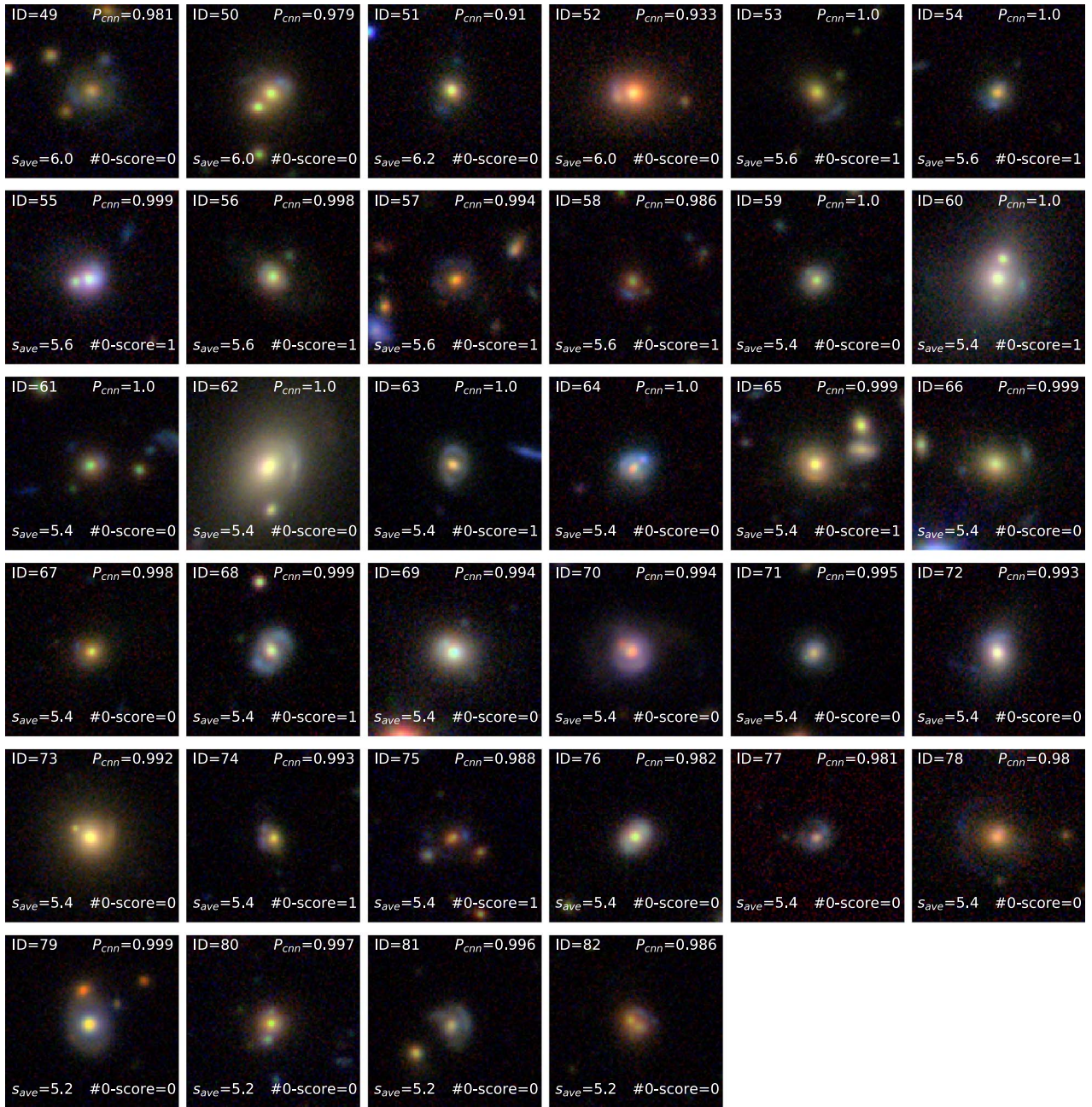**Figure 8.** (Continued.)

high-quality candidates with P-value $\geqslant 0.5$. Among them, 26 candidates, defined as the "golden sample," have a very high probability of being real lenses and are suitable for follow-up observations. We finally provided a qualitative comparison between the CNN presented here and that presented in P19, showing that the nets have comparable performances. A quantitative, statistical, and more complete comparison will be performed in a forthcoming publication. Moreover, in the future, we also plan to extend the CNN to new upcoming ground-based surveys (e.g., LSST) and space missions (CSST and EUCLID) to find a large number of good strong lens candidates suitable for future spectroscopic confirmation follow-up programs.

ORCID iDs

N. R. Napolitano ⬤ https://orcid.org/0000-0003-0911-8884
C. Tortora ⬤ https://orcid.org/0000-0001-7958-6531
C. Spiniello ⬤ https://orcid.org/0000-0002-3909-6359
L. V. E. Koopmans ⬤ https://orcid.org/0000-0003-1840-0312
Z. Huang ⬤ https://orcid.org/0000-0002-1506-1063
S. Chatterjee ⬤ https://orcid.org/0000-0002-8682-1533
M. Radovich ⬤ https://orcid.org/0000-0002-3585-866X
G. Covone ⬤ https://orcid.org/0000-0002-2553-096X
K. Kuijken ⬤ https://orcid.org/0000-0002-3827-0175

References

Abadi, M., Agarwal, A., Barham, P., et al. 2016, arXiv:1603.04467
Agnello, A., Kelly, B. C., Treu, T., et al. 2015, MNRAS, 448, 1446
Agnello, A., Lin, H., Kuropatkin, N., et al. 2018, MNRAS, 479, 4345
Agnello, A., & Spiniello, C. 2019, MNRAS, 489, 2525
ALMA Partnership, Vlahakis, C., Hunter, T. R., et al. 2015, ApJL, 808, L4
Amendola, L., Appleby, S., Avgoustidis, A., et al. 2018, LRR, 21, 2
Auger, M. W., Treu, T., Bolton, A. S., et al. 2009, ApJ, 705, 1099
Auger, M. W., Treu, T., Bolton, A. S., et al. 2010, ApJ, 724, 511
Barnabè, M., Dutton, A. A., Marshall, P. J., et al. 2012, MNRAS, 423, 1073
Bertin, E., & Arnouts, S. 1996, A&AS, 117, 393
Blandford, R. D., & Narayan, R. 1992, ARA&A, 30, 311
Bolton, A. S., Brownstein, J. R., Kochanek, C. S., et al. 2012, ApJ, 757, 82
Bolton, A. S., Burles, S., Koopmans, L. V. E., et al. 2006, ApJ, 638, 703
Bolton, A. S., Burles, S., Koopmans, L. V. E., et al. 2008, ApJ, 682, 964
Bonvin, V., Courbin, F., Suyu, S. H., et al. 2017, MNRAS, 465, 4914
Brownstein, J. R., Bolton, A. S., Schlegel, D. J., et al. 2012, ApJ, 744, 41
Cao, S., Li, X., Biesiada, M., et al. 2017, ApJ, 835, 92
Chen, W., Kelly, P. L., Diego, J. M., et al. 2019, ApJ, 881, 8
Claeyssens, A., Richard, J., Blaizot, J., et al. 2019, MNRAS, 489, 5022
Closson Ferguson, H., Armus, L., Borne, K., et al. 2009, AAS Meeting, 213, 460.07
Collett, T. E. 2015, ApJ, 811, 20
Collett, T. E., Oldham, L. J., Smith, R. J., et al. 2018, Sci, 360, 1342
Congdon, A. B., & Keeton, C. 2018, Principles of Gravitational Lensing: Light Deflection as a Probe of Astrophysics and Cosmology (Cham: Springer)
Cornachione, M. A., Bolton, A. S., Shu, Y., et al. 2018, ApJ, 853, 148
de Jong, J. T. A., Kuijken, K., Applegate, D., et al. 2013, Msngr, 154, 44
Dobler, G., Keeton, C. R., Bolton, A. S., et al. 2008, ApJ, 685, 57
Eisenstein, D. J., Annis, J., Gunn, J. E., et al. 2001, AJ, 122, 2267
Fukugita, M., Futamase, T., Kasai, M., et al. 1992, ApJ, 393, 3
Gilman, D., Birrer, S., Treu, T., et al. 2018, MNRAS, 481, 819
Hartley, P., Flamary, R., Jackson, N., et al. 2017, MNRAS, 471, 3378
He, K., Zhang, X., Ren, S., et al. 2015, arXiv:1512.03385
Hsueh, J.-W., Enzi, W., Vegetti, S., et al. 2020, MNRAS, 492, 3047
Huang, G., Liu, Z., van der Maaten, L., et al. 2016, arXiv:1608.06993
Ivezić, Ž., Connelly, A. J., VanderPlas, J. T., et al. 2014, Statistics, Data Mining, and Machine Learning in Astronomy (Princeton, NJ: Princeton Univ. Press)
Jacobs, C., Collett, T., Glazebrook, K., et al. 2019, ApJS, 243, 17
Jacobs, C., Glazebrook, K., Collett, T., et al. 2017, MNRAS, 471, 167
Keeton, C. R. 1998, PhD thesis, Harvard Univ.
Khramtsov, V., Sergeyev, A., Spiniello, C., et al. 2019, A&A, 632, A56
Kochanek, C. S. 2020, MNRAS, 493, 1725

Koopmans, L. V. E., Bolton, A., Treu, T., et al. 2009, ApJL, 703, L51
Koopmans, L. V. E., Treu, T., Bolton, A. S., Burles, S., & Moustakas, L. A. 2006, ApJ, 649, 599
Kouw, W. M., & Loog, M. 2018, arXiv:1812.11806
Krizhevsky, A., Sutskever, I., & Advances, G. 2012, Commun. ACM, 60, 84
Kuijken, K., Heymans, C., Dvornik, A., et al. 2019, A&A, 625, A2
La Barbera, F., de Carvalho, R. R., Kohl-Moreira, J. L., et al. 2008, PASP, 120, 681
Lecun, Y., Bottou, L., Bengio, Y., & Haffner, P. 1998, IEEEP, 86, 2278
Lemon, C., Auger, M. W., McMahon, R., et al. 2020, MNRAS, 494, 3491
Li, R., Frenk, C. S., Cole, S., et al. 2017, MNRAS, 468, 1426
Li, R., Shu, Y., Su, J., et al. 2019, MNRAS, 482, 313
Li, R., Shu, Y., & Wang, J. 2018, MNRAS, 480, 431
Marshall, P. J., Verma, A., More, A., et al. 2016, MNRAS, 455, 1171
Metcalf, R. B., Meneghetti, M., Avestruz, C., et al. 2019, A&A, 625, A119
Michalski, R. S. 1986, Machine learning. an Artificial Intelligence approach. Vol. 2 (Los Altos, CA: M. Kaufmann Publication)
Miyazaki, S., Komiyama, Y., Nakaya, H., et al. 2012, Proc. SPIE, 8446, 84460Z
More, A., Verma, A., Marshall, P. J., et al. 2016, MNRAS, 455, 1191
Moster, B. P., Somerville, R. S., Maulbetsch, C., et al. 2010, ApJ, 710, 903
Nightingale, J. W., Massey, R. J., Harvey, D. R., et al. 2019, MNRAS, 489, 2049
Oguri, M., & Marshall, P. J. 2010, MNRAS, 405, 2579
Petrillo, C. E., Tortora, C., Chatterjee, S., et al. 2017, MNRAS, 472, 1129
Petrillo, C. E., Tortora, C., Chatterjee, S., et al. 2019a, MNRAS, 482, 807
Petrillo, C. E., Tortora, C., Vernardos, G., et al. 2019b, MNRAS, 484, 3879
Pourrahmani, M., Nayyeri, H., & Cooray, A. 2018, ApJ, 856, 68
Rawat, W., & Wang, Z. 2017, Neural Computation, 29, 2352
Refsdal, S. 1964, MNRAS, 128, 307
Roy, N., Napolitano, N. R., La Barbera, F., et al. 2018, MNRAS, 480, 1057
Rydberg, C.-E., Whalen, D. J., Maturi, M., et al. 2020, MNRAS, 491, 2447
Schneider, P., Ehlers, J., & Falco, E. E. 1992, Gravitational Lenses, XIV (Berlin: Springer-Verlag)
Schuldt, S., Chirivì, G., Suyu, S. H., et al. 2019, A&A, 631, A40
Schwab, J., Bolton, A. S., & Rappaport, S. A. 2010, ApJ, 708, 750
Seidel, G., & Bartelmann, M. 2007, A&A, 472, 341
Shu, Y., Bolton, A. S., Brownstein, J. R., et al. 2015, ApJ, 803, 71
Shu, Y., Bolton, A. S., Mao, S., et al. 2016, ApJ, 833, 264
Shu, Y., Brownstein, J. R., Bolton, A. S., et al. 2017, ApJ, 851, 48
Sluse, D., Rusu, C. E., Fassnacht, C. D., et al. 2019, MNRAS, 490, 613
Sonnenfeld, A., Treu, T., Gavazzi, R., et al. 2013, ApJ, 777, 98
Spiniello, C., Agnello, A., Napolitano, N. R., et al. 2018, MNRAS, 480, 1163
Spiniello, C., Agnello, A., Sergeyev, A. V., et al. 2019, MNRAS, 483, 3888
Spiniello, C., Koopmans, L. V. E., Trager, S. C., et al. 2011, MNRAS, 417, 3000
Suyu, S. H., Auger, M. W., Hilbert, S., et al. 2013, ApJ, 766, 70
Suyu, S. H., Bonvin, V., Courbin, F., et al. 2017, MNRAS, 468, 2590
The Dark Energy Survey Collaboration 2005, arXiv:astro-ph/0510346
Tortora, C., Napolitano, N. R., Romanowsky, A. J., et al. 2010, ApJL, 721, L1
Treu, T. & SWELLS Team 2012, AAS Meeting, 219, 311.06
Turner, E. L., Ostriker, J. P., & Gott, J. R. 1984, ApJ, 284, 1
Vegetti, S., Lagattuta, D. J., McKean, J. P., et al. 2012, Natur, 481, 341
Wong, K. C., Suyu, S. H., Chen, G. C.-F., et al. 2020, MNRAS, in press (doi:10.1093/mnras/stz3094)
Wong, K. C., Zabludoff, A. I., Ammons, S. M., et al. 2013, ApJ, 769, 52
Zhan, H. 2018, in XLII COSPAR Scientific Assembly (Pasadena, CA), E1.16-4-18